



Three-dimensional foam flow resolved by fast X-ray tomographic microscopy

Christophe Raufaste, Benjamin Dollet, Kevin Mader, Stéphane Santucci,
Rajmund Mokso

► To cite this version:

Christophe Raufaste, Benjamin Dollet, Kevin Mader, Stéphane Santucci, Rajmund Mokso. Three-dimensional foam flow resolved by fast X-ray tomographic microscopy. EPL, European Physical Society/EDP Sciences/Società Italiana di Fisica/IOP Publishing, 2015, 111, pp.38004. <10.1209/0295-5075/111/38004>. <hal-01192711>

HAL Id: hal-01192711

<https://hal-univ-rennes1.archives-ouvertes.fr/hal-01192711>

Submitted on 3 Sep 2015

HAL is a multi-disciplinary open access archive for the deposit and dissemination of scientific research documents, whether they are published or not. The documents may come from teaching and research institutions in France or abroad, or from public or private research centers.

L'archive ouverte pluridisciplinaire **HAL**, est destinée au dépôt et à la diffusion de documents scientifiques de niveau recherche, publiés ou non, émanant des établissements d'enseignement et de recherche français ou étrangers, des laboratoires publics ou privés.

Three-dimensional foam flow resolved by fast X-ray tomographic microscopy

C. RAUFASTE¹, B. DOLLET², K. MADER^{3,4}, S. SANTUCCI⁵ and R. MOKSO⁴

¹ *Université Nice Sophia Antipolis, CNRS, LPMC, UMR 7336, Parc Valrose, 06100 Nice, France*

² *Institut de Physique de Rennes, UMR CNRS 6251, Université de Rennes 1, Campus de Beaulieu, 35042 Rennes Cedex, France*

³ *Institute for Biomedical Engineering, University and ETH Zurich, Gloriastrasse 35, Zurich, Switzerland*

⁴ *Swiss Light Source, Paul Scherrer Institute, Villigen, Switzerland*

⁵ *Laboratoire de Physique, ENS Lyon, UMR CNRS 5672, 46 allée d'Italie, 69007 Lyon, France*

PACS 83.80.Iz – Emulsions and foams

Abstract – Adapting fast tomographic microscopy, we managed to capture the evolution of the local structure of the bubble network of a 3D foam flowing around a sphere. As for the 2D foam flow around a circular obstacle, we observed an axisymmetric velocity field with a recirculation zone, and indications of a negative wake downstream the obstacle. The bubble deformations, quantified by a shape tensor, are smaller than in 2D, due to a purely 3D feature: the azimuthal bubble shape variation. Moreover, we were able to detect plastic rearrangements, characterized by the neighbor-swapping of four bubbles. Their spatial structure suggests that rearrangements are triggered when films faces get smaller than a characteristic area.

Foam rheology is an active research topic [1–4], motivated by applications in ore flotation, enhanced oil recovery, food or cosmetics [5]. Because foams are opaque, imaging their flow in bulk at the bubble scale is challenging. To bypass this difficulty, 2D flows of foams confined as a bubble monolayer, which structure is easy to visualize, have been studied. However, the friction induced by the confining plates may lead to specific effects [6], irrelevant for bulk rheology. In 3D, diffusive-wave spectroscopy has been used to detect plastic rearrangements [7, 8]. These events, called T1s, characterized in 2D by the neighbor swapping of four bubbles in contact, are of key importance for flow rheology, since their combination leads to the plastic flow of foams. Magnetic resonance imaging has also been used to measure the velocity field in 3D [9]. However, both these techniques resolve neither the bubble shape, nor the network of liquid channels (Plateau borders, PBs) within a foam. In contrast, X-ray tomography renders well its local structure. However, the long acquisition time of a tomogram, over a minute until very recently, constituted its main limitation, allowing to study only slow coarsening processes [10, 11].

Here, we report the first quantitative study of a 3D foam flow around an obstacle. Such challenge was tackled

thanks to a dedicated ultra fast and high resolution imaging set-up, recently developed at the TOMCAT beam line of the Swiss Light Source [12]. High resolution tomogram covering a volume of $4.8 \times 4.8 \times 5.6 \text{ mm}^3$ with a voxel edge length of $5.3 \text{ }\mu\text{m}$ could be acquired in around 0.5 s, allowing to follow the evolving structure of the bubbles and PB network. Our image analysis shows that the 3D foam flow around a sphere is qualitatively similar to the 2D flow around a circular obstacle: we reveal an axisymmetric velocity field, with a recirculation zone around the sphere in the frame of the foam, and a negative wake downstream the obstacle. Bubble deformations are smaller (in the diametral plane along the mean direction of the flow z) than for a 2D flow, thanks to the extra degree of freedom allowing an azimuthal deformation: bubbles appear oblate before, and prolate after, the obstacle. Finally, we were able to detect plastic rearrangements, characterized by the neighbor-swapping of four bubbles and the exchange of two four-sided faces. Our observations suggest that those events are triggered when the bubble faces get smaller than a characteristic size around R_c^2 , given by a cutoff length of the PB $R_c \simeq 130 \text{ }\mu\text{m}$ in the case of our foam.

Experimental set-up – We prepared a foaming solution following the protocol of [13]: we mixed 6.6% of sodium

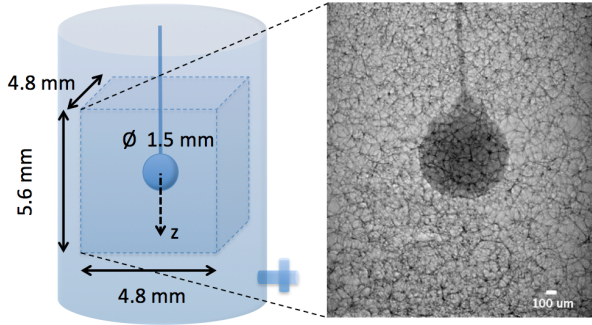


Fig. 1: A plastic bead of 1.5 mm diameter glued to a capillary is placed in the middle of the cylindric chamber of 22 mm diameter and 50 mm height. The acquired tomograms cover the central region with a volume of $4.8 \times 4.8 \times 5.6 \text{ mm}^3$. A typical X-ray projection image is shown on the right.

lauryl ether sulfate (SLES) and 3.4% of cocamidopropyl betaine (CAPB) in mass in ultrapure water; we then dissolved 0.4% in mass of myristic acid (MAc), by stirring and heating at 60°C for one hour, and we diluted 20 times this solution. A few mL of solution was poured in the bottom of a cylindrical perspex chamber of diameter 22 mm and height 50 mm. Bubbling air through a needle immersed in this solution, a foam was created until it reached the top of the chamber. The bottom of the cell contains a tube connected to the open air and closed by a tap. Controlling the opening of the tap, we could obtain a slow steady flow of the liquid foam. Its mean velocity determined a posteriori by image analysis is equal to $v_{\text{flow}} = 8 \mu\text{m/s}$. While flowing, the foam is deformed due to the presence of an obstacle, a smooth plastic bead of diameter $2a = 1.5 \text{ mm}$, attached to a capillary to fix its position in the middle of the chamber (Fig. 1). Because the cell makes a full rotation in 0.5 s, the foam experiences centrifugal acceleration, but it remains below 0.5 m/s^2 within the observation window, hence negligible compared to gravity.

The experiments were performed at the TOMCAT beamline of the Swiss Light Source. Filtered polychromatic X-rays with mean energy of 30 keV were incident on a custom made flow cell (Fig. 1) attached to the tomography stage with three translational and a rotational degrees of freedom. The X-rays passing through the foam in the chamber were converted to visible light by a $100 \mu\text{m}$ thick LuAG:Ce and detected by a 12 bit CMOS camera. Typically 550 radiographic projections acquired with 1 ms exposure time at equidistant angular positions of the sample were reconstructed into a 3D volume of $4.8 \times 4.8 \times 5.6 \text{ mm}^3$ with isotropic voxel edge length of $ps = 5.3 \mu\text{m}$. Such a 3D snapshot of the flowing foam is acquired in $t_{\text{scan}} = 0.55 \text{ s}$, ensuring that motion artifacts are absent since $t_{\text{scan}} < ps/v_{\text{flow}}$. In order to follow the structural changes of the foam during its flow around the obstacle, we recorded a tomogram every 35 seconds for approximately 20 minutes (resulting in around 36 tomograms). The tomograms quality is enhanced using not only the X-rays attenuation by the sample, but also the phase shift

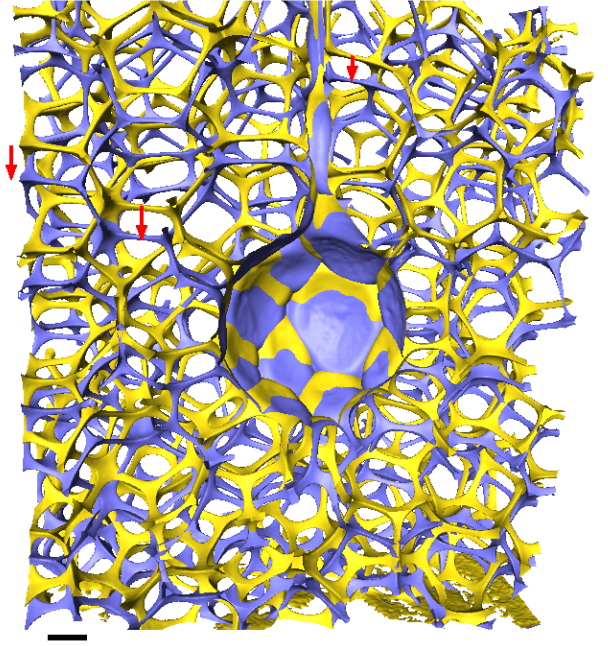


Fig. 2: 3D volume representation of two instances in the foam flow. The PBs and vertices are colored in yellow and blue for time steps t_0 and $t_0 + 35 \text{ s}$ respectively. The scale bar is $300 \mu\text{m}$. Red arrows indicate the flow direction.

of the partially coherent X-ray beam as it interacts with the foaming solution in the PBs and senses the electron density variation in the sample [12]. This phase shift was retrieved using a single phase object approximation [14].

Image analysis – The tomograms are then segmented, separating the PBs and vertices from air. Fig. 2 shows two successive time steps of the 3D snapshots of the reconstructed PBs network during the foam flow around the sphere. We measured the liquid fraction from the segmented images, by computing the relative surface occupied by the PBs and vertices on individual horizontal slices. We measured an averaged liquid fraction of 4% over a tomogram, which did not evolve significantly during our experiments.

Then, we reconstructed and identified individual bubbles of the flowing foam, following the procedure we recently developed and validated on static foam samples, imaged at the same acquisition rate and spatial resolution [15]. We did not observe any evolution of the size distribution of the polydisperse foam studied here, with an average volume $V = 0.36 \pm 0.13 \text{ mm}^3$, hence coarsening remains negligible. Typically, 160 bubbles are tracked between two successive 3D snapshots, leading to statistics over 5600 bubbles. Bubbles smaller than 0.01 mm^3 cannot be discriminated from labeling artifacts [15], and thus, are discarded.

Velocity field – From the bubble tracking, we could measure their velocity \vec{V} around the obstacle. Statistics are performed in the diametral (ρz) plane of the cylindrical coordinates ($\rho\phi z$). We have checked that our results do not

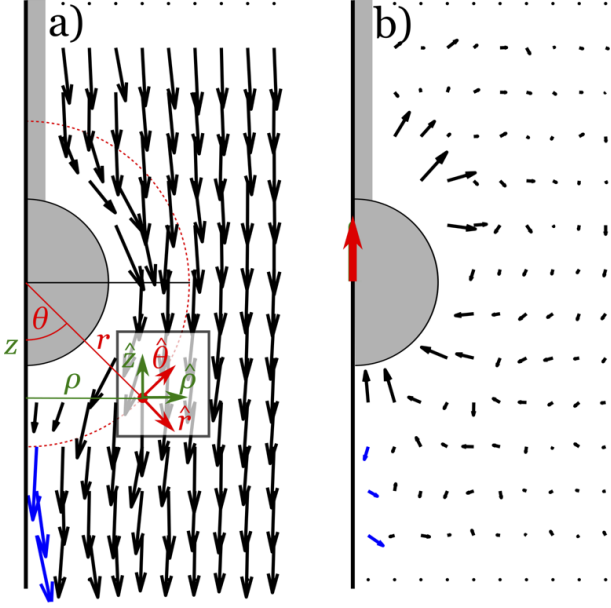


Fig. 3: Velocity fields in the (ρz) plane, (a) in the lab frame. Both the (ρz) or the $(r\theta)$ polar coordinates can be used. The unit vectors $(\hat{\rho}, \hat{z})$ or $(\hat{r}, \hat{\theta})$ are plotted for $r = 1.5$ mm in the plane. The normalized velocity field obtained by subtracting the mean flow velocity is shown in (b). The gray half-disc represents the obstacle (diameter 1.5 mm). The red arrow centered on the semi-obstacle gives the velocity scale of $8 \mu\text{m/s}$. Blue arrows show the negative wake effect.

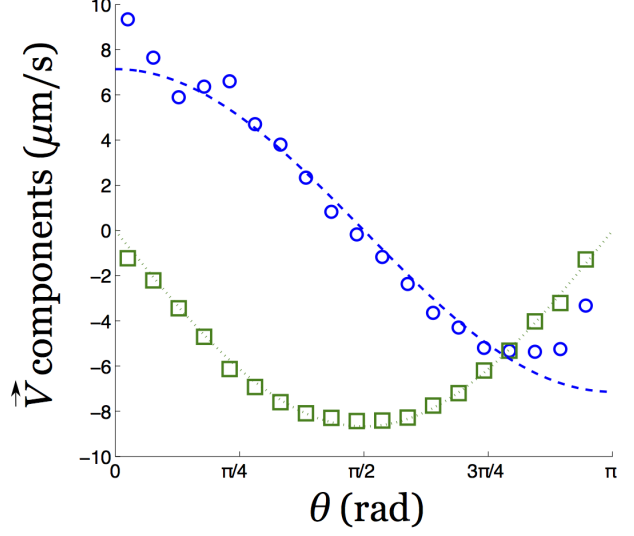


Fig. 4: Velocity components measured at a distance $r = 1.5$ mm from the obstacle center as a function of the polar angle θ : V_r (blue circles) and V_θ (green squares) in the $(r\theta)$ frame. The lines hold for a potential flow model.

depend significantly on the angular coordinate ϕ (see also below), and we have averaged over this coordinate, as well as over time, thanks to the steadiness of the flow. The diametral plane is meshed into rectangular boxes ($0.25 \times 0.40 \text{ mm}^2$). Consistently with the angular averaging procedure, we have checked that the number of bubbles analyzed per box is roughly proportional to the distance of the box to the symmetry axis (data not shown). Averages are weighted by the bubble volumes.

The velocity field is plotted in Fig. 3. In average over all patches, the ϕ -component of the averaged velocity vector is 50 times smaller than its ρz -component, hence the flow is axisymmetric. As expected, the velocity is uniform far from the obstacle, its amplitude decreases close to the leading and trailing points of the sphere, and increases along its sides. Accordingly, there is a clear recirculation zone surrounding the obstacle in the frame of the flowing foam (Fig. 3b). It is worth noting that, compared to 2D foam flows around a circular obstacle [16–19], the range of influence of the obstacle on the flow field is smaller.

Interestingly, there is a zone downstream the obstacle and close to the symmetry axis where the streamwise velocity component is larger than the mean velocity or, equivalently, where the velocity opposes that of the obstacle in the frame of the flowing foam. This reminds the so-called *negative wake*, revealed in viscoelastic fluids [20–22] and also evidenced in 2D foams [17]. However, a difficulty intrinsic to the 3D axisymmetric geometry is

that the statistics is poor in these boxes close to the symmetry axis (about 10 bubbles per box over the full run), and should be improved in the future. The strong fore-aft asymmetry of the flow evidenced by this negative wake confirms that the foam cannot be modelled as a viscoplastic fluid, which gives a fore-aft-symmetric flow [23]: it is intrinsically viscoelastoplastic.

To further quantify the velocity field, its components V_r and V_θ at a distance $r = 1.5$ mm (one obstacle diameter) from the obstacle center are plotted as a function of θ in Fig. 4. We have checked that choosing another distance (e.g. $r = 2$ mm) does not change the qualitative features of the velocity field. The component V_θ is negative, because $\hat{\theta}$ is directed upstream. $|V_\theta|$ is maximum at $\theta = \pi/2$, and V_θ is almost fore-aft symmetric (i.e. symmetric with respect to the axis $\theta = \pi/2$). The component V_r is positive for $\theta < \pi/2$, and negative for $\theta > \pi/2$. Contrary to V_θ , V_r is fore-aft asymmetric. The absolute value of V_r monotonously grows on both sides away from $\pi/2$ (albeit with noise near 0), it reaches a local extremum near $3\pi/4$ then decreases as θ increases towards π . To further reveal this asymmetry, a comparison is made with a potential flow model, which velocity field writes [24]: $V_r = U(1 - r^3/a^3) \cos \theta$, and $V_\theta = -U(1 + r^3/2a^3) \sin \theta$, where U is the uniform velocity far from a spherical obstacle of diameter $2a$. We proceed as follows: first, we fit V_θ with U as the sole free fitting parameter. This procedure gives the dotted line on Fig. 4, with $U = 8.2 \mu\text{m/s}$. We then use this value of U in the potential flow formula for V_r , and we plot it as a dashed line in Fig. 4. While V_θ is very similar to the potential flow case (which is expected, since this only tests its fore-aft symmetry), V_r exhibits deviations from potential flow close to $\theta = 0$ and π . In particular, V_r reaches a value significantly larger than U

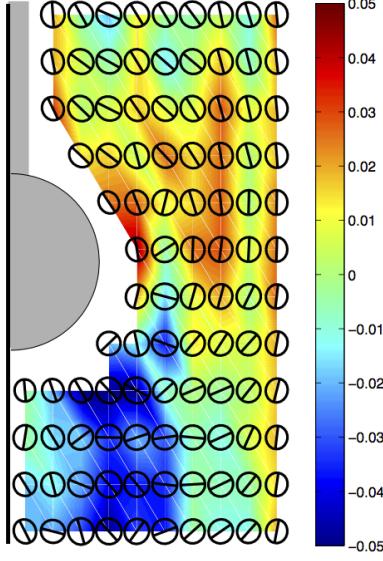


Fig. 5: Projection of the bubble deformation field in the (ρz) plane. Ellipses of bubbles are dilated by a factor of 0.5. The colormap gives the amplitude of the normalized deformation in the azimuthal direction.

close to $\theta = 0$, which is a signature of the negative wake. The deviation close to $\theta = \pi$ is more difficult to interpret, and might be due to the presence of the capillary holding the obstacle

Bubble deformation – Given the set of coordinates $\{\mathbf{r}\}$ of the voxels inside a bubble, we define its inertia tensor $\mathbf{I} = \langle (\mathbf{r} - \langle \mathbf{r} \rangle) \otimes (\mathbf{r} - \langle \mathbf{r} \rangle) \rangle$, and its shape tensor as $\mathbf{S} = \mathbf{I}^{1/2}$. This operation is valid because \mathbf{I} (and hence \mathbf{S}) is a symmetric and definite tensor. Alike the velocity field, averages are performed inside boxes to obtain a shape field (Fig. 5). The bubble deformation is quantified by the eigenvectors/values of the shape tensor. In good approximation, two of them ($S_{\rho z}^+$ and $S_{\rho z}^-$) are found inside the (ρz) plane, the other corresponds to the projection of the tensor along the azimuthal direction ($S_{\phi\phi}$). An effective radius is defined by $R_{\text{eff}} = (S_{\rho z}^+ S_{\rho z}^- S_{\phi\phi})^{1/3}$. The bubbles deformation in the (ρz) plane is represented by ellipses of semi-axes $S_{\rho z}^+$ and $S_{\rho z}^-$. The direction of the largest one, $S_{\rho z}^+$, is emphasized by a line across the ellipse (Fig. 5). Deformation in the azimuthal direction is quantified by $(S_{\phi\phi} - R_{\text{eff}})/R_{\text{eff}}$ in colormap. The orientation of the ellipses in the (ρz) plane exhibits a clear trend comparable to the 2D case [17, 25]. They are elongated streamwise on the obstacle side and at the trailing edge. In between, the ellipses rotate 180° to connect these two regions. We noticed that the deformation of the bubbles is much smaller than for a 2D foam with the same liquid fraction [17, 25]. The deformation in the azimuthal direction exhibits dilation/compression up to 5% only. The quantity $(S_{\phi\phi} - R_{\text{eff}})/R_{\text{eff}}$ is positive upstream (oblate shape) to favor the passage around the obstacle (Fig. 5). The third dimension tends therefore to reduce the bubble deformation in the (ρz) plane by increasing the deformation in the azimuthal direction. This effect is opposite down-

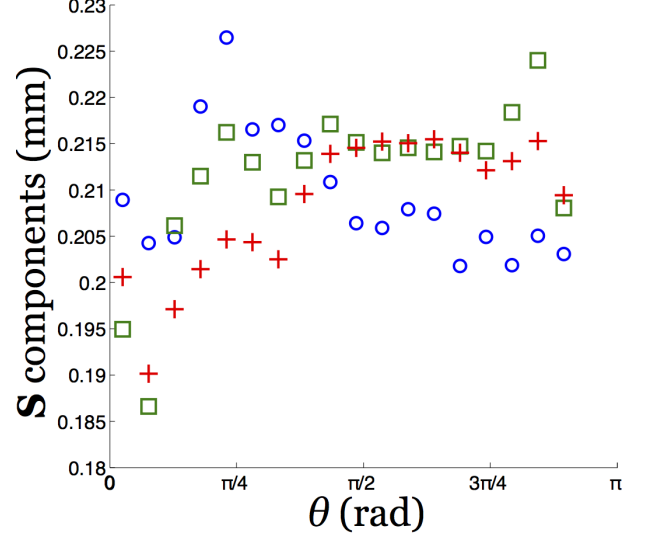


Fig. 6: Shape components measured at a distance $r = 1.5$ mm from the obstacle center as a function of the polar angle θ : S_{rr} (blue circles), $S_{\theta\theta}$ (green squares) and $S_{\phi\phi}$ (red crosses) in the $(r\theta\phi)$ frame. The $S_{r\theta}$ component is approximately 100 times smaller than the other components and is not displayed.

stream, right after the obstacle, where the bubbles are prolate.

These features are further quantified by plotting the normal components of the shape tensor S_{rr} , $S_{\theta\theta}$ and $S_{\phi\phi}$ as a function of θ at $r = 1.5$ mm, in Fig. 6. This graph shows that these normal components remain within a narrow range, between 0.19 mm and 0.22 mm, confirming that the bubbles are weakly deformed. These values correspond to the typical bubble size. For $\theta > \pi/2$ (i.e. upstream the obstacle), S_{rr} is lower than $S_{\theta\theta}$ and $S_{\phi\phi}$, which are approximately equal: hence, the bubbles are squashed against the obstacle. Conversely, for $\theta < 1.2$ rad, S_{rr} is larger than $S_{\theta\theta}$ and $S_{\phi\phi}$: the bubbles are stretched away from the obstacle. Hence, close to the axis $\theta = 0$, the bubbles are elongated streamwise more than spanwise. The origin of the negative wake then becomes clear: by elastically relaxing this deformation, the bubbles “push” the streamlines away from the axis $\theta = 0$. Hence, the velocity has to decrease towards its limiting value U as the bubbles are advected away from the obstacle.

Plastic rearrangements – Automated tracking of bubble rearrangements was hindered by the high sensitivity of such procedure to small defects in the reconstruction of the bubble topology. Description of the contact between bubbles requires to rebuild precisely the faces between bubbles, which would require a finer analysis [26]. Nevertheless, we managed to detect manually four individual events, corresponding to the rearrangements of neighboring bubbles. We provide below a detailed description of one typical example (Fig. 7); the features of the three other ones were found to be the same. Those rearrangements consist of the swapping of four neighboring bubbles, with an exchange of four-sided faces, called T1s

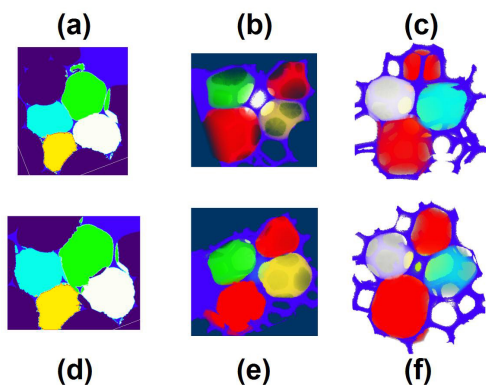


Fig. 7: Example of a T1 in 3D. The white and cyan bubbles lose contact, whereas the green and yellow bubbles come into contact. The red bubbles are the two bubbles that are in contact with these four bubbles over the rearrangement. Three different projections are shown: across the four bubbles that swap neighbors, (a) before and (d) after the T1; (b) in the plane of the face that is about to disappear, and (e) in this plane after the T1; (c) in the plane of the face that is about to appear and (f) in this plane after the T1.

or quadrilateral-quadrilateral (QQ) transitions by Reinelt and Kraynik [27, 28]. We did not observe three-sided faces during a T1 as reported by [29]. These are likely highly unstable, transient states which are too short-lived to be captured by tomography. The QQ transitions observed involve two bubbles losing one face and two bubbles gaining one face. As can be seen on the projection plane across these four bubbles (Fig. 7a and d), this is analogous to T1s in 2D, which always involve four bubbles, two losing one side and two gaining one side. The distance between the two bubbles coming into contact decreases of $150\text{ }\mu\text{m}$, from 1.10 mm before the T1 to 0.95 mm after, while the distance between the two bubbles losing contact increases of $200\text{ }\mu\text{m}$, from 1.03 mm before the T1 to 1.23 mm after. We checked that the distances between the other bubbles around this T1 change much less. This corroborates the vision of a T1 quite similar as in 2D, acting as a quadrupole in displacement, with most effect on the bubbles in the plane. On the other hand, the variation of shape anisotropy of the bubbles involved in the T1 did not show significant trends.

We went further on in the characterization of the spatial structure of those rearrangements. Bubble faces comprise a thin film surrounded by a thick network of PBs and vertices. We have observed that the thin film part is usually very small for faces that are about to disappear, or that have just appeared, during a rearrangement. However, due to the finite radius of the PBs and of the finite size of the vertices, the “skeleton” of these faces is not arbitrarily small. Quantitatively, we measured on the images a PB radius $R_c = 130\text{ }\mu\text{m}$. We also measured the area of the skeleton of the faces on 2D projections along the plane of the faces (we did not observe significantly non-planar faces). We always found skeleton areas larger than

$3.4 \times 10^4\text{ }\mu\text{m}^2$, which is of the order of R_c^2 . This suggests an interesting analogy with the cut-off edge length in 2D foams expected in theory [30, 31], and measured in both simulations [32] and experiments [16]. In 2D foams and emulsions, when the distance between two approaching vertices reaches a certain length, a rearrangement occurs. This happens usually when the two PBs decorating the two neighboring vertices start to merge; hence, the order of magnitude of the cut-off length is R_c . For 3D foams, our observations suggest that there is a cut-off *area* of the order of R_c^2 below which a face becomes unstable, triggering a rearrangement.

In summary, we have provided the first experimental measurement of a 3D time- and space-resolved foam flow measured directly from individual bubble tracking, with novel results on all the essential features of liquid foam mechanics: elasticity, plasticity and flow, through descriptions of shape field, T1 events, and velocity field. Such experimental results could be achieved thanks to the recent advances of both high resolution and fast X-ray tomography and quantitative analysis tools. We discovered differences between 2D and 3D flows in that the range of influence of the obstacle on the flow field is smaller in the 3D case. The same is true for the deformation of the bubbles which is much smaller in the 3D case. Perspectives include further refinements of the analysis tools [15, 26], to fully automatize the detection of rearrangements, to increase statistics and to study various geometries. Imaging the 3D flow at the bubble scale may shed new light on pending issues on shear localization [9] and nonlocal rheology [33].

* * *

We thank Gordan Mikuljan from SLS who realized the experimental cells, Marco Stampanoni for supporting this project, the GDR 2983 Mousses et Émulsions (CNRS) for supporting travel expenses, François Graner, Gilberto L. Thomas and Jérôme Lambert for discussions and the Paul Scherrer Institute for granting beam time to perform the experiments.

REFERENCES

- [1] WEAIRE D. and HUTZLER S., *The Physics of Foams* (Oxford University Press) 1999.
- [2] CANTAT I., COHEN-ADDAD S., ELIAS F., GRANER F., HÖHLER R., PITOIS O., ROUYER F. and SAINT-JALMES A., *Foams, Structure and Dynamics* (Oxford University Press) 2013.
- [3] COHEN-ADDAD S. and HÖHLER R. and PITOIS O., *Annu. Rev. Fluid Mech.*, **45** (2013) 241.
- [4] DOLLET B. and RAUFASTE C., *C. R. Physique*, **15** (2014) 731.
- [5] STEVENSON P., *Foam Engineering: Fundamentals and Applications* (Wiley) 2012.
- [6] WANG Y., KRISHAN K. and DENNIN M., *Phys. Rev. E*, **73** (2006) 031401.

- [7] DURIAN D. J., WEITZ D. A. and PINE D. J., *Science*, **252** (1991) 686.
- [8] COHEN-ADDAD S. and HÖHLER R., *Phys. Rev. Lett.*, **86** (2001) 4700.
- [9] OVARLEZ G., KRISHAN K. and COHEN-ADDAD S., *Europhys. Lett.*, **91** (2010) 68005.
- [10] LAMBERT J., CANTAT I., DELANNAY R., MOKSO R., CLOETENS P., GLAZIER J. A. and GRANER F., *Phys. Rev. Lett.*, **99** (2007) 058304.
- [11] LAMBERT J., MOKSO R., CANTAT I., CLOETENS P., GLAZIER J. A., GRANER F. and DELANNAY R., *Phys. Rev. Lett.*, **104** (2010) 248304.
- [12] MOKSO R., MARONE F. and STAMPANONI M., *AIP Conf. Proc.*, **1234** (2010) 87.
- [13] GOLEMANOV K., DENKOV N. D., TCHOLAKOVA S., VETHAMUTHU M. and LIPS A., *Langmuir*, **24** (2008) 9956.
- [14] PAGANIN D., MAYO S. C., GUREYEV T. E., MILLER P. R. and WILKINS S. W., *J. Microsc.*, **206** (2002) 33.
- [15] MADER K., MOKSO R., RAUFASTE C., DOLLET B., SANTUCCI S., LAMBERT J. and STAMPANONI M., *Colloids Surf. A*, **415** (2012) 230.
- [16] RAUFASTE C., DOLLET B., COX S., JIANG Y. and GRANER F., *Eur. Phys. J. E*, **23** (2007) 217.
- [17] DOLLET B. and GRANER F., *J. Fluid Mech.*, **585** (2007) 181.
- [18] MARMOTTANT P., RAUFASTE C. and GRANER F., *Eur. Phys. J. E*, **25** (2008) 371.
- [19] CHEDDADI I., SARAMITO P., DOLLET B., RAUFASTE C. and GRANER F., *Eur. Phys. J. E*, **34** (2011) 1.
- [20] HASSAGER O., *Nature*, **279** (1979) 402.
- [21] ARIGO M. T. and MCKINLEY G. H., *Rheol. Acta*, **37** (1998) 307.
- [22] HARLEN O. G., *J. Non Newtonian Fluid Mech.*, **109** (2002) 411.
- [23] BERIS A. N., TSAMOPOULOS J. A., ARMSTRONG R. C. and BROWN R. A., *J. Fluid Mech.*, **158** (1985) 219.
- [24] GUYON E., HULIN J. P. and PETIT L., *Hydrodynamique physique* (CNRS Éditions) 2001.
- [25] GRANER F., DOLLET B., RAUFASTE C. and MARMOTTANT P., *Eur. Phys. J. E*, **25** (2008) 349.
- [26] DAVIES I. T., COX S. J. and LAMBERT J., *Colloids Surf. A*, **438** (2013) 33.
- [27] REINELT D. A. and KRAYNIK A. M., *J. Fluid Mech.*, **311** (1996) 327.
- [28] REINELT D. A. and KRAYNIK A. M., *J. Rheol.*, **44** (2000) 453.
- [29] BIANCE A. L., COHEN-ADDAD S. and HÖHLER R., *Soft Matter*, **5** (2009) 4672.
- [30] PRINCEN H. M., *J. Colloid Interface Sci.*, **91** (1983) 160.
- [31] KHAN S. A. and ARMSTRONG R. C., *J. Rheol.*, **33** (1989) 881.
- [32] COX S. J., DOLLET B. and GRANER F., *Rheol. Acta*, **45** (2006) 403.
- [33] GOYON J., COLIN A., OVARLEZ G., AJDARI A. and BOCQUET L., *Nature*, **454** (2008) 84.